IEEE Access
Multidisciplinary | Rapid Review | Open Access Journal

Received June 6, 2019, accepted June 19, 2019, date of publication June 24, 2019, date of current version July 15, 2019.

Digital Object Identifier 10.1109/ACCESS.2019.2924802

Minimum-Entropy Autofocusing Based on Re-PSO for Ionospheric Scintillation Mitigation in P-Band SAR Imaging

LEI YU, YONGSHENG ZHANG, QILEI ZHANG, YIFEI JI, (Student Member, IEEE), AND ZHEN DONG

College of Electronic Science and Technology, National University of Defense Technology, Changsha 410073, China

Corresponding author: Yongsheng Zhang (zyscn@163.com)

This work was supported in part by the National Natural Science Foundation of China (NSFC), under Grant 61501477.

ABSTRACT The spaceborne synthetic aperture radar (SAR) system working at P-band, is vulnerable to the ionospheric effect. The ionospheric scintillation will introduce random phase fluctuations into the SAR signal and deteriorate the imaging performance. In this paper, a minimum-entropy autofocusing method based on the intelligent optimization strategy is proposed to compensate for the scintillation phase error in spaceborne P-band SAR images. A refined particle swarm optimization (Re-PSO) is proposed to provide an intelligent strategy in SAR autofocusing. Compared with the traditional minimum-entropy autofocusing methods, the proposed Re-PSO algorithm is a heuristic method which has extremely strong exploring abilities to the global optimum. The genetic multi-crossover operator and the gradient accelerator are utilized to improve the convergence property of the basic PSO. Furthermore, since the isolate strong scatterers are not required in minimum-entropy SAR autofocusing, the proposed method has strong robustness. The simulations on point and area targets validate the effectiveness and better performance of the proposed method.

INDEX TERMS Autofocusing, ionosphere, P-band, particle swarm optimization (PSO), synthetic aperture radar (SAR), scintillation, minimum-entropy.

I. INTRODUCTION

The P-band synthetic aperture radar (SAR) maintains outstanding capabilities in penetration which can be widely applied in biomass measurement, agriculture observation and military surveillance [1]–[3]. Represented by the BIOMASS system, a tendency of developing the spaceborne P-band SAR system has risen up for the past few years [4].

The spaceborne SAR signal propagating through the ionosphere electron density irregularities suffers the ionospheric deterioration, including the background ionosphere effect and the scintillation [5]–[9]. The background ionospheric effect can be effectively compensated by the prior knowledge of the total electron content [10], [11] or by other technologies [12], [13]. The ionospheric scintillation which is introduced by small scale irregularities (less than 10 km), typically occurs at equator and polar regions, from sunset until midnight [14], [15]. The scintillation-induced signal amplitude and phase fluctuations will introduce signal decorrelation within the synthetic aperture and further degrade the azimuth resolution. As a consequence of the randomness of the scintillation phase error, a data-driven autofocusing method is highly required in P-band SAR scintillation mitigation. The scintillation phase error which is usually considered as a phase screen, shows spatial variation both in range and azimuth. In our work, the spatial variation is dealt with the image segmentation along the range.

In previous works, the phase gradient autofocusing (PGA) which is proposed to estimate the motion phase error in airborne SAR imaging [17] is well studied. The autofocusing performance of PGA highly depends on the isolated strong scatters in SAR images. However, the scintillation effect leads to the rise of the peak side lobe ratio (PSLR) and the integral side lobe ratio (ISLR) of point scatters. This will weaken the SAR image contrast and make it more difficult to select the strong scatters in scintillation-contaminated images. Consequently, the robust of PGA algorithm is limited in SAR scintillation mitigation. J. Chen and Z. Li reported that the PGA

The associate editor coordinating the review of this manuscript and approving it for publication was Venkata Ratnam Devanaboyina.

algorithm is not effective anymore when the signal-to-clutter ratio (SCR) is lower than 16 dB [18]. It is widely acknowledged that the well-focused SAR image has the lower image entropy than the defocusing SAR image. Thus, the minimum-entropy criterion is also widely applied in SAR and inverse SAR (ISAR) autofocusing [19]–[25]. In Wang's work [22], the derivative of the image entropy function is applied to minimize the image entropy. However, in real applications, this algorithm is easy to meet the premature convergence and get stuck in local optima. The Newton optimization method is applied by T. Zeng to minimize the SAR image entropy by calculating the second-order derivative of image entropy function [23] and the same idea is utilized to mitigate the scintillation in GEO SAR imaging [24]. This algorithm only works when the second-order derivative is positive and it is also unable to escape from the local minimum. In J. Wang's work [25], an adaptive-order polynomial phase model is introduced to minimize the SAR image entropy through the iteration, however the parameter optimization strategy is not efficient in [25]. Since the random of the scintillation phase error, a high-order polynomial phase model is required for compensation. For this reason, an intelligent and efficient optimization strategy is required to deal with the huge search space and time complexity.

The previous research built the foundation of our work, but the improvements still need to be accomplished to make the algorithm intelligent and parallel computational. In this paper, the scintillation mitigation is modeled as an optimization problem by using the image entropy function as the objective function. The goal of optimization is to minimize the image entropy by correcting the SAR image with the compensation phase. The parametric model is applied for the compensation phase and this will significantly reduce the dimensions of search space. A refined particle swarm optimization (Re-PSO) method is proposed for the polynomial compensation phase model to optimize its parameters. The PSO is a heuristic optimal algorithm inspired by the social behavior in bird flocks [26]–[28]. During the evolution of swarm, the particles explore the search space driven by the individual and social knowledge. In the swarm, each particle has the "position" and the "fitness" properties. In our work, the position of particles is defined as the parameters of the polynomial phase model and the fitness is defined as the corresponding image entropy. Since each particle has the independent searching ability, the PSO is suitable for parallel computation which makes it more efficient. Finally, the point and area target simulations are performed to present a comprehensive validation of the effectiveness of the proposed algorithm.

II. MINIMUM-ENTROPY AUTOFOCUSING FOR SAR IMAGES WITH SCINTILLATION EFFECT

A. SCINTILLATION EFFECT AND SAR IMAGE ENTROPY

The ionospheric scintillation is produced by small-scale electron density irregularities in the ionosphere. The turbulence of ionospheric irregularities will introduce phase and amplitude fluctuations into the tranionospheric SAR signals. In recent papers, a statistical research based on the Advanced Land Observing Satellite / Phased Array type L-band Synthetic Aperture Radar (ALOS/PALSAR) equatorial images reports that nearly 14 % of the observed images are contaminated by scintillation effect [15], [16]. The geometry of the spaceborne SAR and the scintillation phase screen is shown in Figure 1, where H_{sat} is the height of the radar platform and H_{iono} is the equivalent height of the phase screen which is set as 350 km. As the radar beam scanning over the phase screen within the acquisition time, the phase error is introduced when the signal penetrates the phase screen.

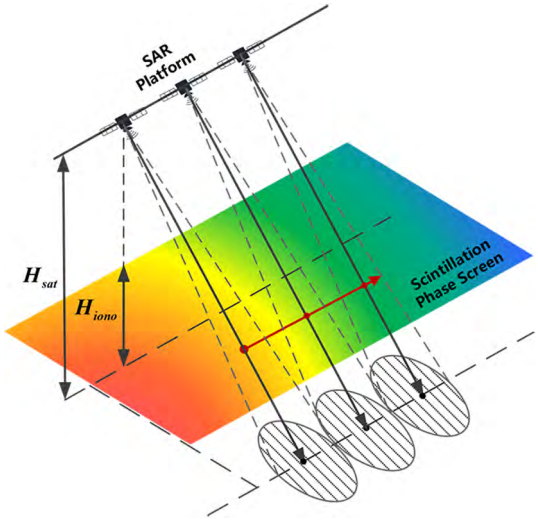

FIGURE 1. The observation geometry of spaceborne SAR with ionospheric scintillation phase screen.

The scintillation phase error within the synthetic aperture leads to the signal decorrelation and the azimuth defocusing. Since the well-focused SAR image has lower entropy, the minimum-entropy criterion is applied to carry out the autofocusing. Like other autofocusing methods, our work also assumes that the phase error is the same in different range positions and compensates the azimuth phase error with a single filter. Actually, the scintillation phase screen shows spatial variation both in range and azimuth. In real applications, the SAR image is segmented into several patches along the range to limit the spatial variation. The minimum-entropy autofocusing guarantees the algorithm can well adapt to each image patch, because it doesn't need to select the strong scatters. The phase compensation on SAR image is performed in range-Doppler domain as follow

$$g(m,n) = \frac{1}{M} \cdot \sum_{k=0}^{M-1} G'(k,n) \times \exp\left(j\left(\Phi(k) - \hat{\varphi}(k)\right)\right) \exp\left(j\frac{2\pi}{M}mk\right) \quad (1)$$

where m and n are the indexes of image in the azimuth and range time domain. M and N are the azimuth and range samples. $\Phi(k)$ and $\hat{\varphi}(k)$ are the ionospheric scintillation phase

error and the compensation phase, respectively. $G'(k,n)$ is the SAR signal before compensation in range-Doppler domain and k is the index of Doppler frequency. The SAR image entropy is expressed as follow

$$E(g) = \ln S - \frac{1}{S}\sum_{m=1}^{M}\sum_{n=1}^{N}|g(m,n)|^2 \ln|g(m,n)|^2 \quad (2)$$

$$S = \sum_{m=1}^{M}\sum_{n=1}^{N}|g(m,n)|^2 \quad (3)$$

where $E(g)$ is the SAR image entropy and S is a constant which represents the power of image. Above all, the aim of our work is to minimize the image entropy by searching and compensating the scintillation phase error.

B. POLYNOMIAL MODEL FOR COMPENSATION PHASE

Based on the aforementioned discussion, the minimum-entropy autofocusing can be considered as an optimization problem, which is described as follow

$$\hat{\boldsymbol{\varphi}} = \arg\min_{\hat{\boldsymbol{\varphi}}}\left[E_g\left(\hat{\boldsymbol{\varphi}}\right)\right]_{M\times 1} \quad (4)$$

where the compensation phase $\hat{\boldsymbol{\varphi}} = \left[\hat{\varphi}_1,\ldots,\hat{\varphi}_k,\ldots,\hat{\varphi}_M\right]$ is a M-dimensional vector and the azimuth sample M can be several thousand for a real SAR image. However, a M-dimensional optimization is not operational because the searching space of parameters is too big which will cause an unendurable waste of time. As a consequence, a parametric polynomial model is applied to fit the compensation phase which is expressed as follow

$$\hat{\boldsymbol{\varphi}} = \sum_{d=2}^{D}\alpha_d \frac{f_a^d}{\max\left(f_a^d\right)} \quad (5)$$

where D is the highest order of polynomial and α_d is the coefficient of the d_{th} order phase. $f_a = \left[-\frac{PRF}{2},\ldots,0,\ldots,\frac{PRF}{2}\right]_{M\times 1}$ is the Doppler frequency sequence. The zero and first order terms are ignored because these terms will not lead to the azimuth defocusing. The $\max\left(f_a^d\right)$ is utilized as the denominator to normalize the high-order phase term which will improve the sensitivity of the algorithm to the variation of the polynomial coefficients. By using the polynomial model in (5), the dimension of search space is significantly decreased from M to D, which makes the algorithm operational.

III. REFINED PARTICLE SWARM OPTIMIZATION

A. THE BASIC PSO ALGORITHM

The particle swarm optimization takes the inspiration from the cognitive ability and the social behavior of the bird and fish flocks. The swarm is a multi-agent distributed system organized by particles (swarm individuals). The evolution of particle is motivated by its individual and social cognition. All the particles tend to move towards the position with better fitness and finally converge to the global optimum in search space. In this paper, the position of the i_{th} particle is defined as $\boldsymbol{\alpha_i} = [\alpha_{i1},\alpha_{i2},\ldots,\alpha_{iD}]_{D\times 1}$ which is the coefficient sequence of phase polynomial. The fitness of particle is defined as the value of the image entropy, so the better fitness means the lower image entropy in this paper (The aim of the algorithm is to search the global minimum). The update of particle's velocity and position in iteration follows

$$\begin{cases}\mathbf{v_i^{k+1}} = \omega\mathbf{v_i^k} + c_1\xi\left(\mathbf{p_{best}^k} - \boldsymbol{\alpha}_i^k\right) + c_2\eta\left(\mathbf{g_{best}^k} - \boldsymbol{\alpha}_i^k\right)\\ \boldsymbol{\alpha}_i^{k\mathcal{C}1} = \boldsymbol{\alpha}_i^k + \mathbf{v_i^{k+1}}\end{cases} \quad (6)$$

where $\mathbf{v_i^k}$ and $\mathbf{v_i^{k+1}}$ are the velocity of particle in k_{th} and $(k+1)_{th}$ iteration, respectively. $\mathbf{p_{best}^k}$ and $\mathbf{g_{best}^k}$ are the "personal best" and the "global best" positions. $\mathbf{p_{best}^k}$ refers to the position of individual best fitness in history and $\mathbf{g_{best}^k}$ is the position of global best fitness in history. c_1 and c_2 are the learning factors (also called acceleration coefficient) which govern the acceleration ability towards the personal best position and the global best position. c_1 controls the self-learning ability as well as c_2 controls the social-learning ability. ω is called the inertia weight which keeps the particle maintaining its velocity in the previous iteration. ξ and η are the random numbers generated from a uniform distribution in [0, 1]. Some literatures [30]–[32] have claimed that a dynamical adjustment of inertia weight and learning factors may dramatically improve the convergence properties of PSO. In this paper, the inertia weight and the learning factors are calculated as follow

$$\begin{cases}c_1 = \left(c_{1f} - c_{1i}\right)\cdot\dfrac{iter}{Iter\_\max} + c_{1i}\\ c_2 = \left(c_{2f} - c_{2i}\right)\cdot\dfrac{iter}{Iter\_\max} + c_{2i}\\ \omega_i = \omega_{\max} - \dfrac{\omega_{\max}-\omega_{\min}}{Iter\_\max}\times iter\end{cases} \quad (7)$$

where $iter$ is the number of current iteration and $Iter\_\max$ is the max iteration time. In this paper, we set $c_{1f} = 1.5$, $c_{1i} = 2.5$, $c_{2f} = 2.5$, $c_{2i} = 1.5$, an asynchronous time-varying learning factor enables the particles to obtain the better exploration ability at the beginning of iteration and the better exploitation performance in the final stage. The inertia weight parameters are set as $\omega_{\max} = 0.9$ and $\omega_{\min} = 0.4$. A linear decreasing inertia weight will lead to overall lowest errors [30].

B. GRADIENT ACCELERATOR

Like other evolution optimization algorithms, the basic PSO algorithm searches the parameter space by using particle swarm with the random strategy without considering the mathematical properties of the problem. However, in practical cases, the gradient of the objective function may contains the important information. Inspired by the steepest descent algorithm [33], the opposite gradient is the steepest descent direction of the objective function which can serve as an accelerator in evolution.

In our experiment, we found that the basic PSO without gradient acceleration will increase the blindness during the evolution. It will finally lead to a huge waste of time

$$\frac{\partial E_g(\alpha_i)}{\partial \alpha_{id}} = \frac{1}{S \cdot M} \cdot \mathrm{Im}\left\{ \sum_{k=0}^{M-1} \left(\frac{f_a^d}{\max\left(f_a^d\right)} \right) \sum_{n=1}^{N-1} G(k,n) \sum_{m=0}^{M-1} \left[1 + \ln |g|^2 \right] \cdot g^* \cdot \exp\left(j \frac{2\pi}{M} mk \right) \right\} \tag{9}$$

and the particles may fail to converge into the global optimum at the end of iteration. Consequently, the gradient information of the image entropy function is utilized in our algorithm to make the particle's evolution more effective and pertinence. The gradient of objective function corresponds to the particle's position is described as $\nabla E_g(\boldsymbol{\alpha_i}) = \left[\frac{\partial E_g(\alpha_i)}{\partial \alpha_{i1}}, \frac{\partial E_g(\alpha_i)}{\partial \alpha_{i2}}, \ldots, \frac{\partial E_g(\alpha_i)}{\partial \alpha_{iD}} \right]^T$. Based on (2) $\sim$ (5), the first order derivative of the image entropy function corresponds to the d_{th} order coefficient in $\boldsymbol{\alpha_i}$ is given as follow

$$\frac{\partial E_g(\boldsymbol{\alpha_i})}{\partial \alpha_{id}} = \frac{1}{S} \sum_{m=1}^{M} \sum_{n=1}^{N} \left[1 + \ln |g(m,n)|^2 \right] \frac{\partial |g(m,n)|^2}{\partial \alpha_{id}} \tag{8}$$

where α_{id} is the d_{th} order coefficient in $\boldsymbol{\alpha_i}$. Since $|g(m,n)|^2 = g^*(m,n)\, g(m,n)$, and $G(k,n) = G'(k,n) \cdot \exp\left(-j\hat{\varphi}(k)\right)$, where $g^*(m,n)$ is the conjugate of $g(m,n)$ and $G'(k,n)$ is the range-Doppler domain expression of $g'(m,n)$ in last iteration. The gradient of the objective function is derived from (9), as shown at the top of this page, which is illustrated at the bottom of this page. The particles are updated along the opposite gradient direction with a specific probability in iterations. The step length is obtained from the one-dimensional search. In this paper, the parabolic method is applied to obtain the optimal step length. With the gradient acceleration, the effectiveness and convergence capability of the algorithm are highly improved.

C. GENETIC MULTI-CROSSOVER OPERATOR AND TABU SEARCH

The basic PSO also suffers the premature convergence which is mainly caused by the rapid flow of pheromone in the swarm. Consequently, many literatures have been proposed to improve the original PSO, such as Dynamic Multi Swarm PSO [34], and Comprehensive Learning PSO [35]. In our work, the genetic multi-crossover operator is applied to increase the diversity of the swarm when the algorithm is trapped in local minimum or tends to immovable. The genetic multi-crossover is proposed in [36]. This operator is firstly applied to determine some parameters in a controller design problem. The principles of the multi-crossover operator are just like the gene exchange between different chromosomes, which is expressed as follow

$$\chi_1' = \chi_1 + \eta\left(2\chi_1 - \chi_2 - \chi_3\right) \tag{10}$$

where χ_1, χ_2, χ_3 are the ''chromosomes'' of particles which are randomly selected from the swarm. In our work, the chromosome refers to the particle's position. We define that χ_1 is selected as the premier parent which has the worst fitness among the selected chromosomes. The chromosome χ_1 is updated by (10). This operator will increase the diversity of the swarm and help some of the particles escape from the local optimum. When the algorithm gets stuck into the local optimum, the multi-crossover operator is introduced to dominate some of the particles' evolution with a specific probability. In this paper, we design that if the algorithm loops over 10 times without finding a better solution then this operator is introduced.

During the evolution, the particles may step into some local areas with very bad fitness, which can be regarded as the ''marsh'' in search space. To prevent the particles from stepping into the marsh area for the second time, the tabu search is applied to help the particles keep away from the area with bad fitness. If the particle does not satisfy the tabu criterion, its information will be recorded in the tabu list and its velocity will be updated by (11). In the next iteration, we will check all the particles if their positions are too close to the recorded data in the tabu list. The local minimum positions are also recorded in the tabu list to prevent the other particles being trapped again. The punished particle will update its velocity by (11) instead of directly being removed from the swarm.

$$\boldsymbol{v_{iL}^{kC1}} = c_1 \xi \left(p_{best}^k - \boldsymbol{\alpha_{iL}^k} \right) + c_2 \eta \left(g_{best}^k - \boldsymbol{\alpha_{iL}^k} \right) \tag{11}$$

Here we drop the inertia term in (6) and only keep the cognitive and learning parts. Note that the tabu list has a limited length and needs to be updated. When the tabu list overflows, the old records will be replaced by the new data. By utilizing the multi-crossover operator and the tabu search, the performance of the Re-PSO is highly improved than the basic PSO algorithm.

D. STRUCTURE OF THE Re-PSO ALGORITHM

In PSO, each particle is defined as an independent individual with self and social cognition. In our experiment, each particle is defined as a class type variable which has four attributes defined as *P.position*, *P.velocity*, *P.fitness* and *P.pbest*. Among them, *P.position* and *P.velocity* are the particle's position and velocity in the current iteration, respectively. *P.fitness* represents the particle's fitness and *P.pbest* is the particle's best position in history. The swarm is also defined as a class type variable which contains *S.pool*, *S.population*, *S.gbest*, *S.fitness* and *S.gb_fitness*. *S.pool* is a list which contains all the particles and *S.gbest* is the global best position of the swarm in history. *S.population* is the swarm population. *S.fitness* is the global best fitness in the current iteration and *S.gb_fitness* is the global best position in history which is calculated by *S.gbest*. These two attributes are used to determine if the image correction is needed in current iteration (obviously, the phase compensation will only be performed when a better solution is found). ω, c_1 and

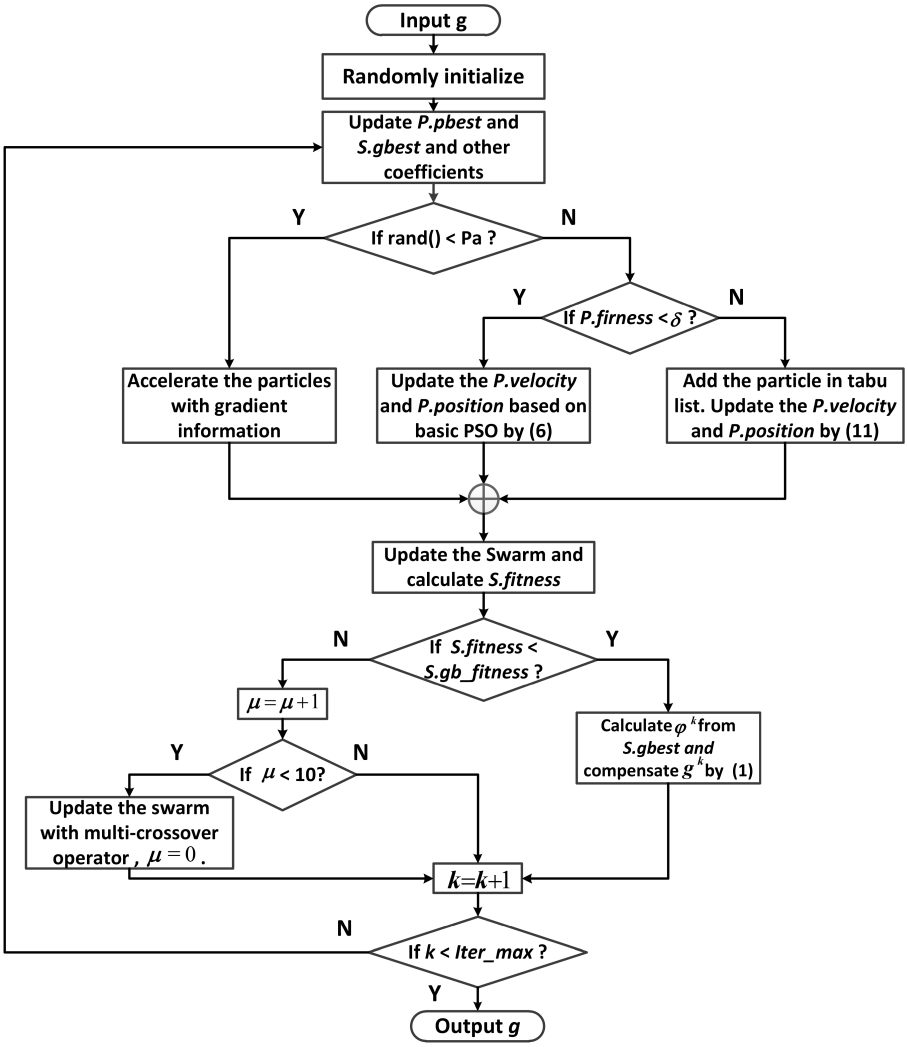

FIGURE 2. The flowchart of the proposed Re-PSO algorithm.

c_2 are the factors calculated in iteration. P_a and P_b are the probabilities of particles to be selected for the gradient accelerator and the multi-crossover operator. Note that since the image entropy is regarded as the particle's fitness, the lower entropy corresponds to better fitness. In other words, our aim is searching the lowest fitness in the search space. The flowchart of the proposed Re-PSO algorithm for scintillation mitigation is shown in Figure 2 and the detailed process is described in pseudocode as follow:

IV. SIMULATION

A. SCINTILLATION PHASE SCREEN SIMULATION

The ionospheric scintillation is caused by the ionospheric irregularities in Fresnel scale. The stochastic dispersion happens to the radar waves when they penetrate the small scale ionospheric irregularities. Since the random propagation of refracted radio waves in ionospheric irregularities, the scintillation shows significant randomness and spatial variation. Consequently, the ionospheric scintillation is simulated by its power spectrum based on the phase screen theory. The Rino power law spectrum [37] has been proved by real measured data and also used in the global ionospheric scintillation model (GISM). Therefore, in this paper, the Rino power law spectrum and SAR scintillation simulator proposed by Carrano [29] are applied to simulate the scintillation effect. The Rino's power spectral density is described as follow

$$\Phi(\boldsymbol{\kappa}) = \frac{r_e^2 \lambda^2 \sec^2(\theta) \cdot C_s L \cdot a \cdot b}{\left[q_0 + \left(A\kappa_x^2 + B\kappa_x\kappa_y + C\kappa_y^2\right)\right]^{(p+1)/2}} \tag{12}$$

$$C_s L = C_k L \left(\frac{2\pi}{1000}\right)^{p+1} \tag{13}$$

where λ is the wavelength of SAR signal and r_e is the classical electron radius. L_0 is the outer scale and $q_0 = 2\pi / L_0$ is the corresponding wave number. Both $C_s L$ and $C_k L$ are the indexes of scintillation strength and their relationship

Algorithm 1 Minimum-Entropy Autofocusing Based on Re-PSO

Require: Input Image: g; Particles: $P.velocity$, $P.position$, $P.pbest$, $P.fitness$; Swarm: $S.pool$, $S.gbest$, $S.population$, $S.fitness$, $S.gb\_fitness$.

function PSO.initialize( )
end function
function PSO.implement(Swarm)
  Set $Iter\_max$, P_a, P_b, δ, $k = 0$, $\mu = 0$.
  for $k = 1 : Iter\_max$ **do**
    Update $P.pbest$, $P.fitness$.
    Calculate inertia weight ω_i and learning factors c_1, c_2 by (7).
    if rand(0,1) < P_a **then**
      Calculate $\boldsymbol{\rho} = -\nabla E\ (\boldsymbol{\alpha})$ by (9) and search the step length λ by parabolic method.
      Based on steepest decent theory, $P.velocity = \lambda \times \boldsymbol{\rho}$, $P.position = P.position + \lambda \times \boldsymbol{\rho}$
    else if $P.fitness < \delta$ **then**
      Update the $P.velocity$ and $P.position$ as basic PSO by (6).
    else
      Push the particle into tabu list and update the $P.velocity$ and $P.position$ by (11).
    end if
    Add all the particles into $S.pool$ and update $S.fitness$.
    if $S.fitness < S.gb\_fitness$ **then**
      $S.gb\_fitness \leftarrow S.fitness$, calculate φ^k with $S.gbest$ by (5) and compensate g^k by (1).
    else
      $\mu = \mu + 1$
      if $\mu > 10$ **then**
        Update the swarm by multi-crossover operator with P_b and set $\mu = 0$.
      end if
    end if
    $k = k + 1$
  end for
end function

is shown in (12). p is the spectral index and θ is the incident angle. Both a and b are structural scaling factors of irregularities along and vertical to the magnetic field. A, B and C are the coefficients referring to the transmit direction and the geomagnetic field. Their complete expressions have been detailedly discussed in [29] and we will not make the extension here. What's more, the $\boldsymbol{\kappa} = (\kappa_x, \kappa_y)$ is the transverse wavenumber refers to the penetration point on the phase screen.

The orbit, radar system and the ionospheric parameters are listed in Table 1. The parameter settings refer to the discussion in [15]. Note that the scintillation strength and the spectral index are selected in a range to illustrate a comprehensive verification of the algorithm's performance. A simulation of

TABLE 1. Radar system and ionospheric parameters.

Parameters	Value
Carrier frequency	0.6 GHz
Bandwidth	30 MHz
Azimuth antenna	10 m
Outer scale L_o	10 km
Scintillation strength C_kL	$10^{33} \sim 10^{34}$
Spectral index p	$3 \sim 5$
Structure scale a, b	10, 1
Altitude of radar platform	700 km
Incident angle θ	30 deg

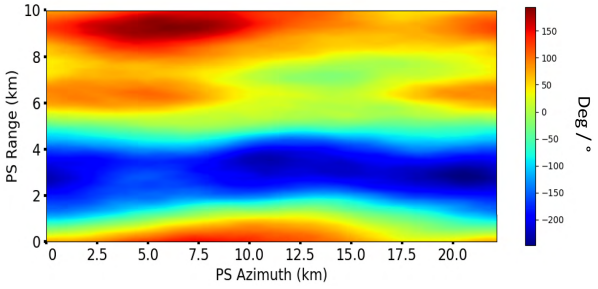

FIGURE 3. A simulation of scintillation phase screen.

TABLE 2. PSO Parameters.

Parameter	Value	Parameter	Value
C_{1f}	1.5	C_{1i}	2.5
C_{2f}	1.5	C_{2i}	2.5
ω_{min}	0.4	ω_{max}	0.9
P_a=P_b	5 %	δ	$2 \cdot S.fitness$
Dimension	15	Swarm population	400

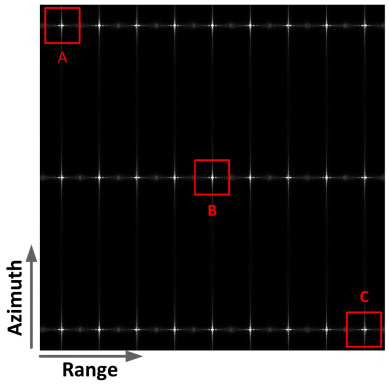

FIGURE 4. The imaging result on point array target.

scintillation phase screen is shown in Figure 3, in the case of $C_kL = 10^{33}$, $p = 5$. As is shown in Figure 3, the scintillation phase screen shows significant spatial variation both in range and azimuth. Thus, the image segmentation is applied along the range to restrict the spatial variation in an endurable level. The simulation methods on area and point target basically follow the description in [29]. The PSO parameters used in

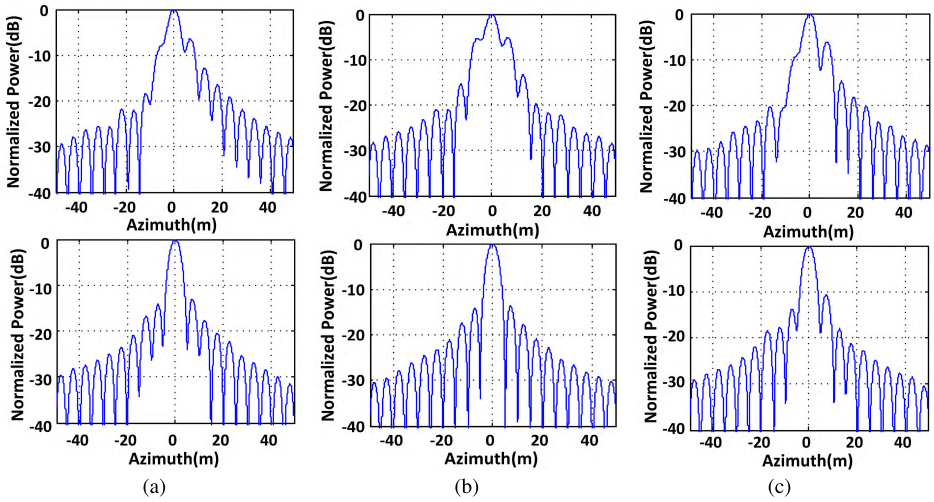

FIGURE 5. The azimuth slices of the scintillation imaging and autofocusing results of target A, B and C. (a) target A before and after autofocusing. (b) target B before and after autofocusing. (c) target C before and after autofocusing.

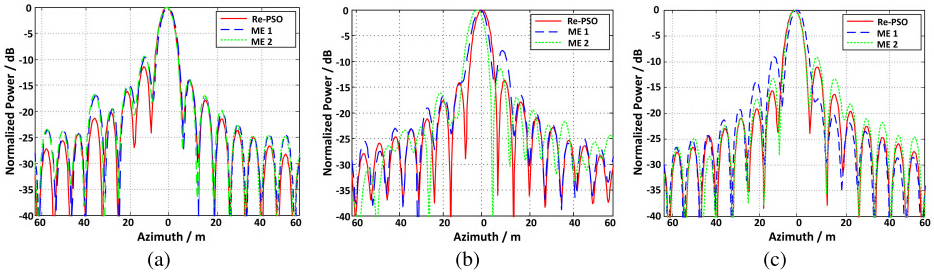

FIGURE 6. Autofocusing performance comparisons between our method and other minimum-entropy autofocusing algorithms. (a) comparison of target A. (b) comparison of target B. (c) comparison of target C.

this paper are listed in Table 2. As is discussed above, the c_1, c_2 and ω dynamically change in iteration. P_a and P_b dominate the probabilities of the gradient accelerator and the multi-crossover operator. The polynomial dimension is defined as $D = 15$ to fit the high order terms in the scintillation phase.

B. POINT TARGET SIMULATION

The point target simulation provides a quantitative analysis of the autofocusing performance of the proposed Re-PSO algorithm. In this section, the autofocusing performance of our method is demonstrated and comparisons with [22] and [24] are presented to verify the advantages of our method. Finally, the Monte-Carlo simulation is performed to find out the effective boundary of the proposed algorithm. The point target simulation is carried out based on a 5 km $\times$ 5 km point array target as is shown in Figure 4. Three point targets locating at different positions are selected to analyze the autofocusing performance of the proposed algorithm. As is shown in Figure 4, the three targets are named as target A, target B and target C, respectively. The ideal azimuth and range resolutions are 4.4807 m and 4.3839 m, respectively. Due to the spatial variation of the scintillation phase screen, each target in Figure 4 suffers different scintillation phase error both in range and azimuth. The azimuth slice of the scintillation imaging and autofocusing results of the three point scatters when $C_k L = 10^{33}$, $p = 5$ are shown in Figure 5.

Since the ionospheric scintillation mainly induces the azimuth degeneration [15], only the azimuth slices are demonstrated in Figure 5. The range segmentation is utilized to restrict the range variation of scintillation phase error. It is obvious that the scintillation-induced azimuth decorrelation leads to the broadening of mainlobe and the asymmetric sidelobe. The distortion in range is not as serious as azimuth, thus the autofocusing only performs along the azimuth. As is shown in Figure 5 (a) and (b), target A and target B are perfectly refocused (Point A: PSLR $= -12.51$ dB ISLR $= -9.63$ dB, Point B: PSLR $= -13.01$ dB ISLR $= -9.93$ dB). For target C in Figure 5 (c), the asymmetric sidelobe still exists in autofocusing result due to the residual high-order phase error. The PSLR and ISLR of target C are -11.43 dB and -9.31 dB, respectively. The autofocusing performance comparisons on these three targets are illustrated in Figure 6. The comparisons are carried

TABLE 3. The statistical data on PSLR, ISLR and azimuth resolution of the point target imaging results from Monte-Carlo simulation.

	Before autofocusing			After autofocusing		
Scintillation Parameters	PSLR (dB)	ISLR (dB)	RES (m)	PSLR (dB)	ISLR (dB)	RES (m)
$p = 3, C_k L = 10^{33}$	-10.935	-8.199	4.442	-12.751	-9.782	4.430
$p = 4, C_k L = 10^{33}$	-9.752	-7.566	4.452	-12.158	-9.993	4.437
$p = 5, C_k L = 10^{33}$	-7.842	-4.852	4.568	-12.093	-9.411	4.433
$p = 3, C_k L = 3 \times 10^{33}$	-10.743	-7.567	4.462	-12.641	-9.413	4.467
$p = 4, C_k L = 3 \times 10^{33}$	-8.602	-6.976	5.286	-12.091	-9.557	4.432
$p = 5, C_k L = 3 \times 10^{33}$	-6.595	-6.110	7.185	-12.239	-9.467	4.450
$p = 3, C_k L = 10^{34}$	-6.561	-5.327	6.045	-10.615	-7.960	4.437
$p = 4, C_k L = 10^{34}$	-6.254	-4.528	7.009	-10.574	-7.848	4.468
$p = 5, C_k L = 10^{34}$	-3.216	-2.642	10.105	-9.468	-7.072	4.432

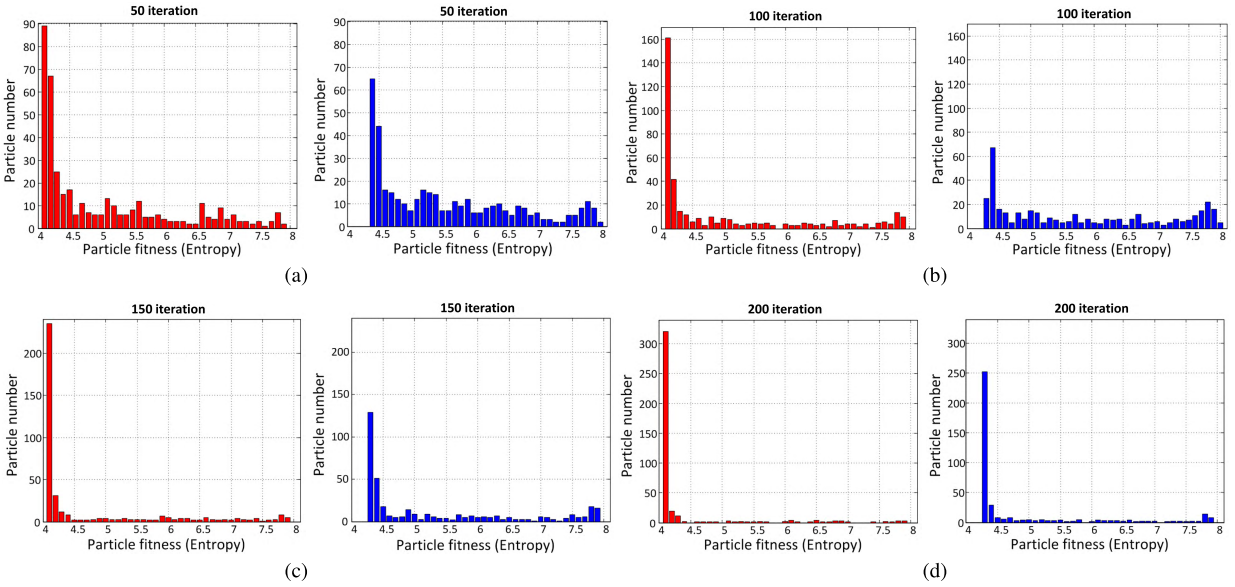

FIGURE 7. The statistical histogram of the particles' fitness (entropy) in different iterations, the red histograms show the results of Re-PSO and the blue histograms show the results of basic PSO. (a) 50 iterations. (b) 100 iterations. (c) 150 iterations. (d) 200 iterations.

out between our method (Re-PSO) and the existing minimum-entropy autofocusing methods proposed in [22] (ME 1) and [24] (ME 2). Note that the same range segmentation strategy is applied for all these three autofocusing methods. Comparing with ME1 and ME2, the proposed Re-PSO method shows better autofocusing performance in these three cases which are demonstrated as the preservation of the mainlobe and the suppression of sidelobes. The comparisons validate that the Re-PSO is able to escape from the local minimum to get better solutions than traditional minimum-entropy autofocusing methods.

The Monte-Carlo simulation is carried out to verify the performance of the proposed algorithm in different scintillation conditions. The simulations are iteratively performed for 100 times in each scintillation condition and the statistical results are illustrated in Table 3. From Table 3, we can know that with the increasing of the scintillation strength and spectral index, the PSLR and ISLR suffer more serious degeneration. The azimuth imaging resolution slightly decreases when $C_k L = 10^{33}$ and dramatically decrease when $C_k L = 10^{34}$. It is shown in Table 3 that the proposed algorithm maintains excellent autofocusing performance when $C_k L \leq 3 \times 10^{33}, p \leq 5$. The PSLR and ISLR of the autofocusing results start to degrade until $C_k L \geq 10^{34}$. However, the improvements of azimuth resolution after autofocusing are still significant even in strong scintillation conditions. The Monte-Carlo simulation validates that the proposed Re-PSO algorithm maintains effectiveness when $C_k L \leq 3 \times 10^{33}$, $p \leq 5$.

Furthermore, the convergence properties of the Re-PSO algorithm proposed in this paper are discussed and validated in Figure 7. In Figure 7, the statistical histograms demonstrate the distribution of the particles' fitness by the Re-PSO and the basic PSO in different iteration. In this case, the ideal SAR image entropy (without scintillation effect) is $E_0 = 3.981$ and the contaminated image entropy (before autofocusing) is $E_{iono} = 4.887$. As is shown in Figure 7 (a), the evolution result of the Re-PSO (red histogram) shows

(a) (b) (c)

FIGURE 8. The area target simulation. (a) original SAR image. (b) scintillation imaging result. (c) autofocusing result with Re-PSO.

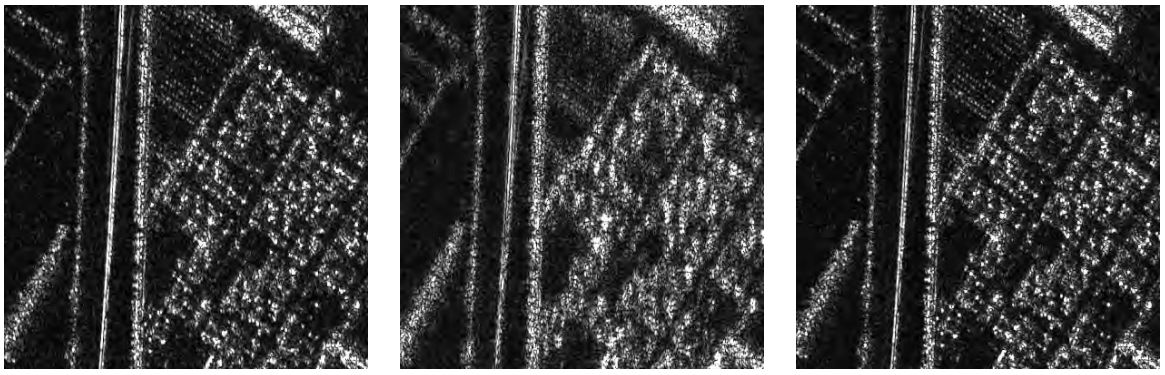

(a) (b) (c)

FIGURE 9. The locally magnified images of the area target simulation. (a) original SAR image. (b) scintillation imaging result. (c) autofocusing result with Re-PSO.

better convergence than the basic PSO in the 50th iteration. This means the gradient accelerator plays an important role in the evolution at early stages. In the following evolution stages, as a consequence of the dynamic inertia weight and learning factors, the particles of the Re-PSO show better exploration performance than the basic PSO. After 150 iterations, most of the particles of the Re-PSO have converged to the global minimum position. However, the convergence performance of the basic PSO is much poorer. The genetic multi-crossover operator is applied to increase the diversity of the swarm with a proper probability when the evolution tends to frozen. The tabu search helps the particles keep away from the bad position and the discovered local minimum. Finally, the Re-PSO converges to $E_{gb} = 4.012$ after 300 iterations comparing with the result $E'_{gb} = 4.162$ after 500 iterations of the basic PSO. These results validate the better autofocusing performance of the Re-PSO proposed in this paper. The comparisons in Figure 7 show that the Re-PSO algorithm has both the better convergence ability and the better autofocusing performance.

C. AREA TARGET SIMULATION

Due to the lack of operating spaceborne P-band SAR system, the area target simulation is carried out by using the radar cross-section (RCS) of an 1000×1000 pixels airborne P-band SAR image acquired in Longmen, China, $35.51N°$, $110.62E°$. A group of low orbit satellite parameters listed in Table 1, are applied to carry out the simulation of a P-band spaceborne SAR system. The ideal imaging result is shown in Figure 8 (a). The simulation of scintillation phase screen follows the descriptions in [30]. The simulation is carried out in the case of $C_kL = 3 \times 10^{33}, p = 4$. The size of the simulating phase screen is 22.40 km in azimuth and 4.43 km in range. As is shown in Figure 3, the spatial phase variation in range cannot be neglected. Consequently, image segmentation is applied to limit the range variation of phase screen. In our work, the segmentation length in range is set as 200 m which will meet the requirements of computation efficiency and autofocusing performance. The scintillation imaging result and the autofocusing result with the proposed Re-PSO algorithm are shown in Figure 8 (b) and Figure 8 (c). The ideal SAR image entropy in Figure 8 (a) is 12.082. The entropy of scintillation-contaminated SAR image and the autofocusing result are 12.468 and 12.114, respectively. The image entropy amelioration validates the effectiveness of the proposed Re-PSO algorithm quantitatively. Comparatively, the autofocusing results of ME1 and ME2 are 12.368 and 12.342 that also indicates the better performance of Re-PSO.

To present a more clear demonstration, the locally magnified images of the scintillation-contaminated SAR image and the autofocusing result are shown in Figure 9. The locally magnified images are selected in the bottom right corner of the scene. It is shown in Figure 9 (b) that the increase of ISLR and PSLR induced by scintillation cause the image blur and the decrease of SAR image contrast. By using the proposed Re-PSO autofocusing algorithm the azimuth blur is refocused and the degeneration of ISLR and PSLR are significantly mitigated.

V. CONCLUSION

The P-band SAR system will be seriously deteriorated by ionospheric scintillation when the radio waves penetrate the ionospheric irregularities. In this paper, an intelligent ionospheric scintillation mitigation method is proposed based on the minimum-entropy autofocusing. The scintillation mitigation is considered as an optimization problem and a Re-PSO algorithm is proposed to provide a heuristic optimal solution. Compared with the traditional optimization method like the Newton method and the steepest descent method, the PSO algorithm provides a cognitive and parallel searching strategy that is able to evade the local minimum. The gradient accelerator and the genetic multi-crossover operator are utilized to improve the convergence ability and prevent the premature convergence. The tabu list is used to punish the bad evolution and prevent the particles from plunging into the local minimum for the second time. Finally, the simulation validates the effectiveness and better autofocusing performance of the proposed method. The Monte-Carlo simulation indicates that the proposed autofocusing method maintains effectiveness in the moderate scintillation condition. We hope this paper may provide a new viewpoint for the scintillation mitigation and the same idea may also be further applied in SAR or ISAR image autofocusing.

REFERENCES

[1] E. Rignot, J. R. Zimmermann, and J. J. van Zyl, "Spaceborne applications of P band imaging radars for measuring forest biomass," *IEEE Trans. Geosci. Remote Sens.*, vol. 33, no. 5, pp. 1162–1169, May 1995.

[2] T. Le Toan, A. Beaudoin, J. Riom, and D. Guyon, "Relating forest biomass to SAR data," *IEEE Trans. Geosci. Remote Sens.*, vol. 30, no. 2, pp. 403–411, Mar. 1992.

[3] M. C. Dobson, F. T. Ulaby, T. LeToan, A. Beaudoin, E. S. Kasischke, and N. Christensen, "Dependence of radar backscatter on coniferous forest biomass," *IEEE Trans. Geosci. Remote Sens.*, vol. 30, no. 2, pp. 412–415, Mar. 1992.

[4] M. Arcioni, P. Bensi, M. W. J. Davidson, M. Drinkwater, F. Fois, C-C. Lin, R. Meynart, K. Scipal, and P. Silvestrin, "ESA's biomass mission candidate system and payload overview," in *Proc. IEEE Int. Geosci. Remote Sens. Symp.*, Munich, Germany, Jul. 2012, pp. 5530–5533.

[5] J. Liu, Y. Kuga, X. Pi, A. Freeman, and A. Ishimaru, "Ionospheric effects on SAR imaging: A numerical study," *IEEE Trans. Geosci. Remote Sens.*, vol. 41, no. 5, pp. 939–947, May 2003.

[6] Z. W. Xu, J. Wu, and Z.-S. Wu, "Potential effects of the ionosphere on space-based SAR imaging," *IEEE Trans. Antennas Propag.*, vol. 56, no. 7, pp. 1968–1975, Jul. 2008.

[7] Y. Ji, Q. Zhang, Y. Zhang, and Z. Dong, "L-band geosynchronous SAR imaging degradations imposed by ionospheric irregularities," *China Sci. Inf. Sci.*, vol. 60, no. 6, Jun. 2017, Art. no. 060308.

[8] Y. Ji, Q. Zhang, Y. Zhang, and Z. Dong, "Analysis of background ionospheric effects on geosynchronous SAR imaging," *Radioengineering*, vol. 26, no. 1, pp. 130–138, Apr. 2017.

[9] Y. Ji, Y. Zhang, Q. Zhang, Z. Dong, and B. Yao, "Retrieval of ionospheric Faraday rotation angle in low-frequency polarimetric SAR data," *IEEE Access*, vol. 7, pp. 3181–3193, 2019.

[10] C. R. Mannix, D. P. Belcher, P. S. Cannon, and M. J. Angling, "Using GNSS signals as a proxy for SAR signals: Correcting ionospheric defocusing," *Radio Sci.*, vol. 51, no. 2, pp. 60–70, Feb. 2016.

[11] W. Xiao, W. Liu, and G. Sun, "Modernization milestone: BeiDou M2-S initial signal analysis," *GPS Solutions*, vol. 20, no. 1, pp. 125–133, Jan. 2016.

[12] G. Gomba, A. Parizzi, F. De Zan, M. Eineder, and R. Bamler, "Toward operational compensation of ionospheric effects in SAR interferograms: The split-spectrum method," *IEEE Trans. Geosci. Remote Sens.*, vol. 54, no. 3, pp. 1446–1461, Mar. 2016.

[13] S. Mancon, D. Giudici, and S. Tebaldini, "The ionospheric effects mitigation in the BIOMASS mission exploiting multi-squint coherence supported by Faraday rotation," in *Proc. 12th Eur. Conf. Synth. Aperture Radar*, Aachen, Germany, Jun. 2018, pp. 1–6.

[14] D. P. Belcher and P. S. Cannon, "Amplitude scintillation effects on SAR," *IET Radar Sonar Navigat.*, vol. 8, no. 6, pp. 658–666, 2014.

[15] F. J. Meyer, K. Chotoo, S. D. Chotoo, B. D. Huxtable, and C. S. Carrano, "The influence of equatorial scintillation on L-band SAR image quality and phase," *IEEE Trans. Geosci. Remote Sens.*, vol. 54, no. 2, pp. 869–880, Feb. 2016.

[16] Y. Ji, Y. Zhang, Q. Zhang, and Z. Dong, "Comments on 'The influence of equatorial scintillation on L-band SAR image quality and phase,'" *IEEE Trans. Geosci. Remote Sens.*, to be published. doi: 10.1109/TGRS.2019.2912450.

[17] P. H. Eichel and C. V. Jakowatz, "Phase-gradient algorithm as an optimal estimator of the phase derivative," *Opt. Lett.*, vol. 14, no. 20, pp. 1101–1103, 1989.

[18] Z. Li, S. Quegan, J. Chen, and N. C. Rogers, "Performance analysis of phase gradient autofocus for compensating ionospheric phase scintillation in BIOMASS P-band SAR data," *IEEE Geosci. Remote Sens. Lett.*, vol. 12, no. 6, pp. 1367–1371, Jun. 2015.

[19] S. Zhang, Y. Liu, and X. Li, "Fast entropy minimization based autofocusing technique for ISAR imaging," *IEEE Trans. Signal Process.*, vol. 63, no. 13, pp. 3425–3434, Jul. 2015.

[20] S. Zhang, Y. Liu, and X. Li, "Autofocusing for sparse aperture ISAR imaging based on joint constraint of sparsity and minimum entropy," *IEEE J. Sel. Topics Appl. Earth Observ. Remote Sens.*, vol. 10, no. 3, pp. 998–1011, Mar. 2017.

[21] S. Zhang, Y. Liu, and X. Li, "Bayesian bistatic ISAR imaging for targets with complex motion under low SNR condition," *IEEE Trans. Image Process.*, vol. 27, no. 5, pp. 2447–2460, May 2018.

[22] J. Wang, X. Liu, and Z. Zhou, "Minimum-entropy phase adjustment for ISAR," *IEE Proc.–Radar, Sonar Navigat.*, vol. 151, no. 4, pp. 203–209, Aug. 2004.

[23] T. Zeng, R. Wang, and F. Li, "SAR image autofocus utilizing minimum-entropy criterion," *IEEE Geosci. Remote Sens. Lett.*, vol. 10, no. 6, pp. 1552–1556, Nov. 2013.

[24] R. Wang, C. Hu, Y. Li, S. E. Hobbs, W. Tian, X. Dong, and L. Chen, "Joint amplitude-phase compensation for ionospheric scintillation in GEO SAR imaging," *IEEE Trans. Geosci. Remote Sens.*, vol. 55, no. 6, pp. 3454–3465, Jun. 2017.

[25] J. Wang and X. Liu, "SAR minimum-entropy autofocus using an adaptive-order polynomial model," *IEEE Geosci. Remote Sens. Lett.*, vol. 3, no. 4, pp. 512–516, Oct. 2006.

[26] J. Kennedy and R. Eberhart, "Particle swarm optimization," in *Proc. IEEE ICNN*, vol. 4. Nov./Dec. 1995, pp. 1942–1948.

[27] M. Meissner, M. Schmuker, and G. Schneider, "Optimized particle swarm optimization (OPSO) and its application to artificial neural network training," *BMC Bioinf.*, vol. 7, no. 1, p. 125, Dec. 2006.

[28] N. Mohammadi and S. J. Mirabedini, "Comparison of particle swarm optimization and backpropagation algorithms for training feed forward neural network," *J. Math. Comput. Sci.*, vol. 12, pp. 113–123, Aug. 2014.

[29] C. S. Carrano, K. M. Groves, and R. G. Caton, "Simulating the impacts of ionospheric scintillation on L band SAR image formation," *Radio Sci.*, vol. 47, no. 4, pp. 1–4, Aug. 2012.

[30] J. Xin, G. Chen, and Y. Hai, "A particle swarm optimizer with multi-stage linearly-decreasing inertia weight," in *Proc. Int. Joint Conf. Comput. Sci. Optim.*, Sanya, China, Apr. 2009, pp. 505–508.
[31] J. C. Bansal, P. K. Singh, M. Saraswat, A. Verma, S. S. Jadon, and A. Abraham, "Inertia weight strategies in particle swarm optimization," in *Proc. 3rd World Congr. Nature Biologically Inspired Comput.*, Salamanca, Spain, Oct. 2011, pp. 633–640.
[32] Y. Feng, G.-F. Teng, A.-X. Wang, and Y.-M. Yao, "Chaotic inertia weight in particle swarm optimization," in *Proc. 2nd Int. Conf. Innov. Comput., Inf. Control (ICICIC)*, Kumamoto, Japan, Sep. 2007, p. 475.
[33] R. Fletcher and C. M. Reeves, "Function minimization by conjugate gradients," *Comput. J.*, vol. 7, no. 2, pp. 149–154, 1964.
[34] J. J. Liang and P. N. Suganthan, "Dynamic multi-swarm particle swarm optimizer," in *Proc. IEEE Swarm Intell. Symp.*, Pasadena, CA, USA, Jun. 2005, pp. 124–129.
[35] J. J. Liang, A. K. Qin, P. N. Suganthan, and S. Baskar, "Comprehensive learning particle swarm optimizer for global optimization of multimodal functions," *IEEE Trans. Evol. Comput.*, vol. 10, no. 3, pp. 281–295, Jun. 2006.
[36] W.-D. Chang, "A multi-crossover genetic approach to multivariable PID controllers tuning," *Expert Syst. Appl.*, vol. 33, no. 3, pp. 620–626, Oct. 2007.
[37] C. L. Rino, "A power law phase screen model for ionospheric scintillation: 2. Strong scatter," *Radio Sci.*, vol. 14, no. 6, pp. 1147–1155, Nov./Dec. 1979.

LEI YU was born in Yanji, Jilin, China, in 1995. He received the B.S. degree in electronic information engineering from the Dalian University of Technology (DUT), Dalian, in 2013. He is currently pursuing the Ph.D. degree with the College of Electronic Science and Technology, National University of Defense Technology (NUDT).

His current major research interests include radar signal processing, synthetic aperture radar, and ionospheric impacts.

YONGSHENG ZHANG was born in Inner Mongolia, China, in 1977. He received the Ph.D. degrees in electronics and information engineering from the National University of Defense Technology, in 2007.

He is currently an Associate Professor with the College of Electronic Science and Technology, National University of Defense Technology. His current major research interests include SAR system design and SAR data processing.

QILEI ZHANG was born in Gansu, China. He received the B.S. degree in communication engineering, and the M.S. and Ph.D. degrees in information and communication engineering from the National University of Defense Technology (NUDT), Changsha, in 2007, 2009, and 2014, respectively.

From 2012 to 2013, he was a visiting Ph.D. student with the University of Birmingham, Birmingham, U.K. He is currently a Lecturer with the National University of Defense Technology. His fields of interests include signal processing, synthetic aperture radar, and ionosphere.

YIFEI JI was born in Jiangyin, Jiangsu, China, in 1992. He received the B.S. degree in electronic information engineering from the Nanjing University of Science and Technology (NUST), Nanjing, in 2014, and the M.S. degree in information and communication engineering from the National University of Defense Technology (NUDT), Changsha, in 2016, where he is currently pursuing the Ph.D. degree with the College of Electronic Science and Technology.

His current research fields of interests include radar signal processing, synthetic aperture radar, and ionospheric impacts.

ZHEN DONG was born in Anhui, China, in 1973. He received the Ph.D. degree in electrical engineering from the National University of Defense Technology (NUDT), Changsha, in 2001, where he is currently a Professor with the College of Electronic Science and Technology.

His current recent research interests include SAR system design and processing, ground moving target indication (GMTI), and digital beamforming (DBF).